

12-1-2008

Measurement of Liquid Water Accumulation in a Proton Exchange Membrane Fuel Cell with Dead-Ended Anode

Jason B. Siegel

University of Michigan, Ann Arbor

Denise A. McKay

University of Michigan, Ann Arbor, dmckahn@smith.edu

Anna G. Stefanopoulou

University of Michigan, Ann Arbor

Follow this and additional works at: https://scholarworks.smith.edu/egr_facpubs



Part of the [Engineering Commons](#)

Recommended Citation

Siegel, Jason B.; McKay, Denise A.; and Stefanopoulou, Anna G., "Measurement of Liquid Water Accumulation in a Proton Exchange Membrane Fuel Cell with Dead-Ended Anode" (2008). Engineering: Faculty Publications, Smith College, Northampton, MA.
https://scholarworks.smith.edu/egr_facpubs/118

This Conference Proceeding has been accepted for inclusion in Engineering: Faculty Publications by an authorized administrator of Smith ScholarWorks. For more information, please contact scholarworks@smith.edu

FuelCell2008-65053

MEASUREMENT OF LIQUID WATER ACCUMULATION IN A PROTON EXCHANGE MEMBRANE FUEL CELL WITH DEAD-ENDED ANODE

Jason B. Siegel, Denise A. McKay, and Anna G. Stefanopoulou
Fuel Cell Control Laboratory, University of Michigan, Ann Arbor, Michigan, 48109
Contact e-mail: siegeljb@umich.edu

ABSTRACT

The operation and accumulation of liquid water within the cell structure of a polymer electrolyte membrane fuel cell (PEMFC) with a dead-ended anode is observed using neutron imaging. The measurements are performed on a single cell with 53 square centimeter active area, Nafion 111-IP membrane and carbon cloth Gas Diffusion Layer (GDL). Even though dry hydrogen is supplied to the anode via pressure regulation, accumulation of liquid water in the anode gas distribution channels was observed for all current densities up to 566 mA cm^{-2} and 100% cathode humidification. The accumulation of liquid water in the anode channels is followed by a significant voltage drop even if there is no buildup of water in the cathode channels. Anode purges and cathode surges are also used as a diagnostic tool for differentiating between anode and cathode water flooding. The rate of accumulation of anode liquid water, and its impact on the rate of cell voltage drop is shown for a range of temperature, current density, cathode relative humidity and air stoichiometric conditions. Neutron imaging of the water while operating the fuel cell under dead-ended anode conditions offers the opportunity to observe water dynamics and measured cell voltage during large and repeatable transients.

1 INTRODUCTION

The electrochemical power generation of a popular category of fuel cells depends on the proton-conducting properties of their polymer electrolyte membranes. The ability of the membrane to conduct protons increases with increasing water content. How-

ever, polymer electrolyte membrane fuel cells (PEMFCs) operate below the boiling point of water causing excess water to condense and restrict gas delivery or block the active fuel cell area. The build-up of water mass, referred to as flooding, in an operating fuel cell was first observed with neutron imaging in [1]. The impact of this flooding phenomena is a recoverable reduction in the power output of the fuel cell stack, seen by a decrease in cell voltage [2, 3], but can also lead to irrecoverable material degradation [4, 5].

This paper presents the neutron imaging of liquid water accumulation in a polymer electrolyte membrane fuel cell (PEMFC) operating with a dead-ended anode. Modeling and testing for anode flooding conditions is rare because most experimental fuel cells operate under flow through conditions for which anode flooding is highly unlikely. However, our adjustable purging schedule applied to a stack with a dead-ended anode can enable high hydrogen utilization and remove the need for costly, heavy, and bulky anode humidification and recirculation hardware.

In dead-ended anode operation, the buildup of liquid water in the channels and Gas Diffusion Layer (GDL) blocks the ability of reactant gases to reach the catalyst layer, resulting in reactant starvation and carbon corrosion [5], which damages the cell over time. A solenoid valve placed downstream from the cell, allows for an occasional purging event with high hydrogen flow rate to remove water from the anode, preventing severe voltage drop and reactant starvation. Optimal scheduling of purge events is necessary to prolong stack life and minimize wasted

hydrogen. Therefore models which accurately predict the accumulation of water are necessary. If in addition to water accumulation, the model can also predict the resulting cell voltage, it could be used in combination with voltage measurement to allow real-time adaptation of the purging events in response to component aging, environmental changes and system faults. Specifically, the estimated voltage is compared with the actual voltage and the error is used to adjust the model-based purge schedule. A similar model-based technique was used for the estimation of hydrogen starvation [6] and control of the hydrogen production rate from a fuel processor [7]. Hence, the experiments and experimental results detailed here, sought to confirm that a consistent correlation between anode channel water accumulation and voltage degradation exists. This data is valuable for calibrating and validating existing models of liquid water dynamics in PEM fuel cells, and the corresponding impact on cell voltage [8–16], due to the large and repeatable transients in voltage and liquid water mass. Despite some limitations of the imaging system [17], with careful cell design and masking, the exact location of the liquid water within the cell structure can be inferred, similar to the work of [2,3,18–23]. During all experiments, the fuel cell system is operated with a dead-ended anode using a pressure regulated supply of dry hydrogen. We also distinguish anode versus cathode channel flooding using controlled cathode surging and anode purging events. During an anode purge, the inlet flow (pure hydrogen) is increased to remove the liquid water stored in the anode. During a cathode surge the air flow is momentarily and abruptly increased beyond the nominal excess ratio to remove any liquid water stored in the cathode.

It is demonstrated that liquid water accumulates in the anode gas channels and this buildup of liquid water is well correlated with the dynamic cell voltage response during the majority of the experiments, as originally predicted in [24]. A similar notion of reduced active area due to liquid water coverage in the anode was recently presented in [25]. Our conclusions about channel water mass are based on several homogeneity assumptions, which ignore the difference in the stored liquid water mass in the GDL under the channels as compared to areas under lands [17, 26]. Nevertheless the data and data analysis provide useful new information regarding PEMFC transient behavior.

2 Experimental Hardware

Experiments were conducted at the Neutron Imaging Facility at the National Institute for Standards and Technology (NIST) Center for Neutron Research [27]. We used the amorphous silicon detector for its 1Hz image acquisition rate, to capture the change in mass of liquid water over time. Aperture setting 3, and beam 1 were used for the experiment, which gives a neutron fluence rate I_0 of $7.2 \times 10^6 \text{ cm}^{-2} \text{ s}^{-1}$ with the ratio of source to detector distance over the source aperture diameter (L/D) equal to 600. The width of a pixel in the image corresponds to $127 \mu\text{m}$, but the resolution of the imaging system is only $250 \mu\text{m}$ as a re-

sult of scintillator blooming [27].

A NIST test stand is used to supply a humidified gas stream to the cathode in flow through operation. A portable anode purging system was constructed, which allows dead-ended operation of the fuel cell. This anode purge system consists of a pressure regulator, which supplies dry hydrogen to the anode inlet, and a solenoid valve downstream of the anode outlet. A needle valve placed downstream from the solenoid valve allows the target flow rate during the anode purge to be controlled. Between purges the anode is supplied with hydrogen via pressure regulation, as shown in Fig. 1. Voltage, current, pressure, temperature and cathode flow rate measurements were recorded continuously at 1 Hz resolution. The image data was selectively recorded when repeatable large transients were observed. Due to the large file size it was not desirable to capture data for all times, creating gaps in the measured liquid water mass data.

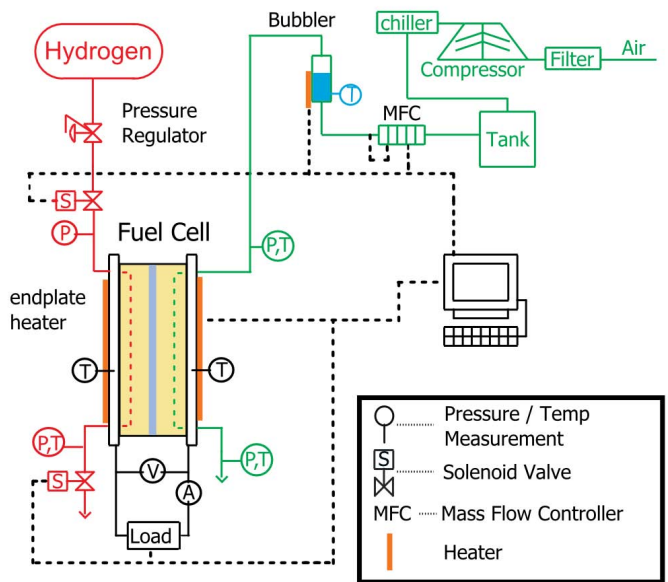


Figure 1. Experimental hardware detailing sensor and actuator locations.

The cell was comprised of a single 53 cm^2 Nafion[®] 111-IP membrane which is $25.4 \mu\text{m}$ thick with anode and cathode catalyst layers containing a Pt areal density of 0.3 mg cm^{-2} purchased from Ion Power. SGL 10BB non-woven carbon gas diffusion layers, were used, which have an uncompressed thickness of $420 \mu\text{m}$ and a porosity of $\epsilon = 0.84$. The cell hardware, purchased from Electrochem, consisted of aluminum endplates, gold coated aluminum current collectors and resin impregnated graphite flow

fields. Resin impregnated graphite is used to prevent liquid water from accumulating inside the pore-structure of the graphite [28]. The graphite plates were thinned to 0.32 cm to reduce neutron attenuation. The anode gas channels are straight with a channel width of 2.08 mm, depth of 1.78 mm, and land width of 0.838 mm. A semi-serpentine flow path is used on the cathode with 5 parallel paths, each having a channel width of 0.686 mm, a channel depth of 0.991 mm and a land width of 0.762 mm. A square 45W resistive heater, with a surface area of 58 cm², was attached to each end plate to ensure uniform heating and maintain the desired temperature at low current density.

3 Quantification of Liquid Water Mass

The attenuation properties of a neutron beam passing through an object can be used to form a projected image on a detector, similar to X-ray radiography. Neutrons are strongly scattered by hydrogen atoms, concentrated in liquid water, and only weakly interact with the other materials used in PEMFCs, such as aluminum and carbon. Therefore, neutron images are sensitive to the amount of liquid water present in the cell. They provide a useful tool for in-situ measurement of liquid water content while employing commercial fuel cell materials with realistic cell designs. The use of these materials reduces the possibility of temperature gradients, induced by selection of non-standard materials, which would otherwise greatly impact the formation of liquid water within the cell.

Figure 2 shows two images collected before and after a purge event. The areas with high liquid water accumulation are clearly visible in the top left frame, which corresponds to a condition before an anode purge event. The second frame in Fig. 2 shows the drier neutron image collected after the purge.

The image, $I(j,k)$, formed by scattering and absorption of neutrons, can be modeled by the Beer-Lambert law

$$I(j,k) = I_0(j,k) \exp \left[- \sum_{l=1}^N \mu_l t_l(j,k) \right], \quad (1)$$

where $I_0(j,k)$ is the incident flux rate of neutrons, N is the number of material layers in the object, t_l is the thickness of each layer, and μ_l is the linear attenuation coefficient of each layer.

In order to quantify the thickness of liquid water, we must determine the amount of attenuation which is caused by water in the image. A section of the image outside the active area, defined by S_p , is used to normalize each image before processing to account for fluctuations in the nuclear reactor power output and $I_0(j,k)$ over time, according to

$$I^{norm}(j,k) = \frac{I(j,k)}{\sum_{j,k \in S_p} I(j,k)}. \quad (2)$$

To reduce systematic error, care was taken to ensure reference images, $I_{dry}^{norm}(j,k)$, were taken of a completely dry cell and

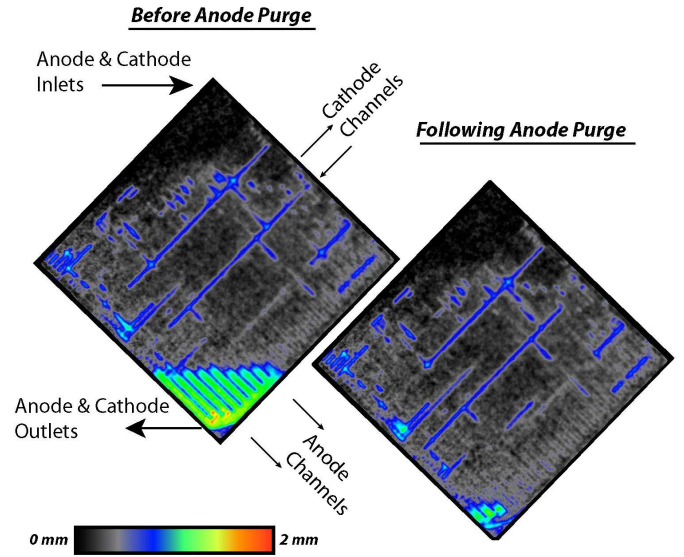


Figure 2. Neutron images of the fuel cell active area before and after an anode purge events, indicating the actual cell orientation. The cell was operated at 566 mA cm⁻², 55 °C, with fully humidified air at a stoichiometry of 200% for cathode and dry hydrogen supplied to anode.

1500 images were averaged to reduce noise in the image. In order to account for the effects of thermal expansion, which cause portions of the cell to move within the imaging frame, dry reference images were taken at 5 °C increments over the operating temperature range of the fuel cell. The relative neutron transmission, found by dividing an image by the dry reference image of the cell, can be used to calculate water thickness assuming that the attenuation caused by everything but liquid water remains unchanged since the reference image was captured. A 3x3 median filter is applied to the images to reduce random noise before calculating the liquid water thickness. The thickness of the water layer was calculated using

$$t_w(j,k) = - \frac{1}{\mu_w} \ln \left[\frac{I^{norm}(j,k)}{I_{dry}^{norm}(j,k)} \right], \quad (3)$$

and the experimentally obtained attenuation coefficient, $\mu_w = 0.3708 \pm 0.0008$ mm⁻¹ [27], which is valid for liquid water thickness less than 1 mm.

Liquid water quantification is further complicated by instrument broadening caused by the scintillator screen, scattering of neutrons by objects in the beam and detector noise [18, 29]. The trends in the data will still be evident without correction for these effects. Quantification of the error introduced by each phenomena is currently under investigation at the NIST [27].

3.1 Temporal Averaging to Reduce Uncertainty

The measured uncertainty in water volume for a single pixel in the detector system sampled at the 1 Hz rate is $0.32 \times 10^{-6} \text{ cm}^3$ using beam 2 and aperture 4 [27], which is different from our setup. The measured uncertainty can be scaled to account for the different neutron flux used in the experiment, beam 1 and aperture 3, by multiplying by the ratio of the square root of the fluence rates, which yields a liquid water volumetric uncertainty of $0.537 \times 10^{-6} \text{ cm}^3$ per pixel. This relationship can be derived from the equation for the theoretical uncertainty [27],

$$\delta_t = \frac{1}{\mu} \sqrt{\frac{1 + e^{\mu t}}{I_o A T \eta}} \approx \frac{1}{\mu} \sqrt{\frac{2}{I_o A T \eta}}, \quad (4)$$

where t is the water thickness, μ is the attenuation coefficient, I_o is the fluence rate, A is the area, T is the integration time, and η is the detector efficiency. Equation (4) also indicates that a reduction in uncertainty of the measured liquid water volume can be achieved, at the expense of temporal resolution by averaging several frames. The uncertainty in an averaged frame of 11 s as compared to 1 s is decreased by a factor of $\sqrt{1/T} \approx 0.3$. Since the time constants associated with liquid water are on the order of 100 s [28, 30], the 11 s imaging rate was used. The resulting liquid water volume uncertainty is $0.16 \times 10^{-6} \text{ cm}^3$ per pixel, which corresponds to a water thickness of $10 \text{ } \mu\text{m}$.

3.2 Masking

The processed water thickness image, $t_w(j, k)$, is a 2-D projection of the liquid water inside the fuel cell. In order to infer the location of liquid water in the third dimension, a knowledge of the physical material structure can be combined with logical arguments. For example liquid water cannot be located within an impervious solid material. Several masking techniques have been used to analyze neutron images [2, 3, 20, 21]. We employ a similar process to estimate the mass of liquid water in three layers; the anode channel, cathode channel and combined membrane and GDL layer (which consists of both anode and cathode GDLs). The masks are formed using the drawings of the graphite plates. Mask A defines the active area of the fuel cell, mask B is for the anode channels and mask C is for the cathode channels. Four mutually disjoint masks, D-G, identify regions of the fuel cell corresponding to the different possible combinations of channels and lands on each side of the membrane as shown in Fig. 3. The area of each mask, and their logical relationships are shown in Table 1. The water thickness in the combined membrane and GDL layer can be directly measured from the images for regions identified by mask G, which contain both anode and cathode lands and therefore water could not be present in either of the other two layers.

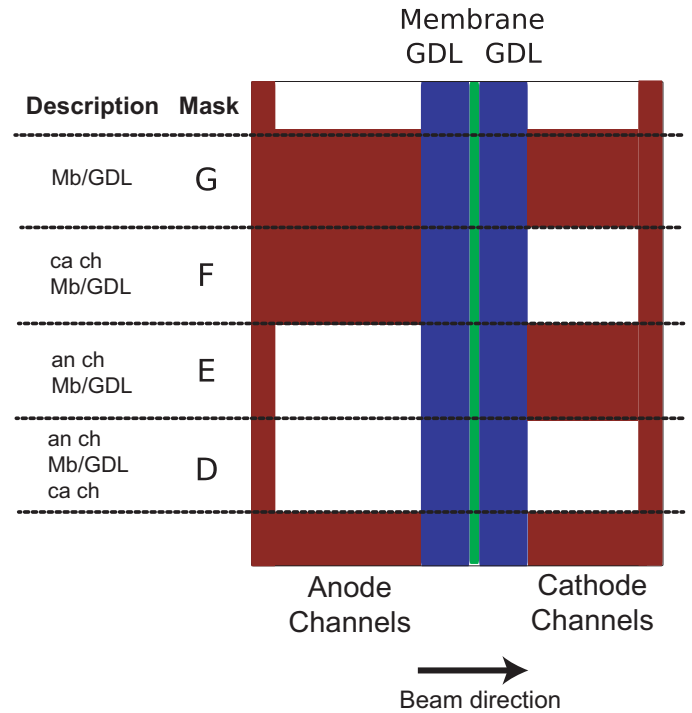


Figure 3. Schematic of fuel cell layers, the beam direction is perpendicular to the membrane which is defined to be the y axis.

Table 1. Masks

Mask	Description	#Pixels	Relationship
A	Active Area	313600	$D \cup E \cup F \cup G$
B	Anode Channel Area	234099	
C	Cathode Channel Area	169392	
D	Both Ch + MEMB + GDL	128047	$B \cap C$
E	An Ch + MEMB + GDL	106052	$(B \cap \bar{C}) \cap A$
F	Ca Ch + MEMB + GDL	41345	$(\bar{B} \cap C) \cap A$
G	MEMB + GDL only	38155	$(\bar{B} \cap \bar{C}) \cap A$
H	Subset of G	11239	$H \subset G$

3.3 Local Spatial Averaging

Estimation of the distribution of liquid water in the third dimension using masking over the entire active area requires consideration of the significant spatial variations in the liquid water thickness along the channels. Therefore, a local 2-D spatial average is constructed. Specifically, the active area is partitioned into a 9×9 grid of 81 segments similar to [3]. A 9×9 grid is chosen corresponding to the nine segments of parallel cathode channels as seen in Fig. 4, which is overlaid on mask C. Within each of the 81 segments, the flow of reactant gases is in the same direc-

tion. Due to a manufacturing error the cathode inlet and outlet manifolds were incorrectly positioned rendering the first and last serpentine flow path ineffective. The cathode inlet should be located in segment 1, for proper operation, but is instead located in segment 9 as shown in Fig. 4. Due to the orientation of the cell, prior to masking, each thickness image is rotated 44.3° to the right using a bi-cubic interpolation method to facilitate registration with the mask. In the rotated orientation, studies can be performed along the channels by traversing the coordinate axis of the image. Note that segment 9, which is highlighted in Fig. 4, corresponds to upper corner of the fuel cell shown in Fig. 2. Segment 9 is also the location of the gas inlets where the dry hydrogen and humidified air enter the anode and cathode channels respectively.

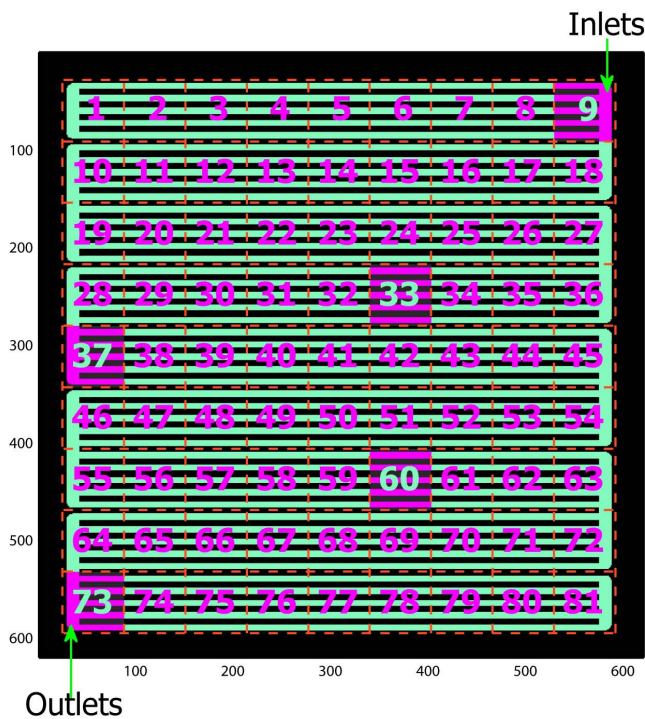


Figure 4. The cathode channel, mask C, is partitioned into 81 segments for the evaluation of the spatial distribution in cathode channel liquid water. Five representative segments are highlighted and shown in later analysis.

The fuel cell conditions are assumed to be uniform within each of the 81 segments. Five image masks (D-H) are applied to each of the 81 segments individually, and the average liquid water thickness in each of the masked regions is calculated for each segment. A fifth mask H, which is a subset of the points in mask G which are not adjacent to either channel, is used to get a more accurate estimate of the water content in the combined

GDL and membrane layer. This mask reduces the effects of instrument broadening and neutron scattering when there is liquid water present in the neighboring channels [18,27].

The top subplot in Fig. 5, shows a comparison of the average water thickness calculated using masks G and H, over the entire active area for the combined membrane and GDL layer. When considering the entire active area, there is little difference between the average water thicknesses when using mask G as compared using mask H. However, for individual segments, a more significant difference between the application of mask G versus mask H is observed, as indicated in the remaining subplots. The largest difference in average thicknesses is found in segment 73, located at the gas outlet near the bottom of the cell. Due to the orientation of the cell and dead-ended anode, liquid water accumulates in this corner of the anode channel because it is forced by the reactant gas flow and gravity. A detailed description of the experimental testing conditions for this experiment can be found in Fig. 6.

The standard deviation in thickness, of points identified by mask G, provides a metric for how uniform the water content in the combined membrane and GDL layer is over that segment shown in Fig. 5. A large standard deviation in thickness may indicate non-uniform conditions in the membrane and/or GDL, or it may be the result of scintillator blurring and/or scattering when a significant amount of water is present in the channel. In the limiting case, when the water thickness is uniform, the standard deviation in measured thickness should be equal to that of the Poisson counting process given by Eqn. (4), which increases with increasing water thickness. The large standard deviation measured for segment 9 between $t=725-800$ mins is likely due to condensation and buildup of liquid water near the cathode inlet manifold. A cathode surge conducted at around $t=780$ min pushes liquid water out of segment 9, reducing the measured standard deviation in that segment. Segment 73 consistently contained the most water and therefore also has the highest standard deviation.

3.4 Channel Liquid Mass

To calculate the mass of liquid water in the gas channels, assume that the water thickness in the combined membrane and GDL layers is uniform over a segment, then it is equal to the averaged thickness in the region defined by mask H. In this case the average liquid water thickness in the anode channel can be estimated by taking the difference between averaged water thickness in masked regions H (MB/GDL) and E (MB/GDL+AnCh) for each segment. Similarly, the average cathode channel liquid water thickness can be estimated by the difference between averaged water thickness in regions H and F. The total estimated liquid water mass in each layer of the cell is found by summing

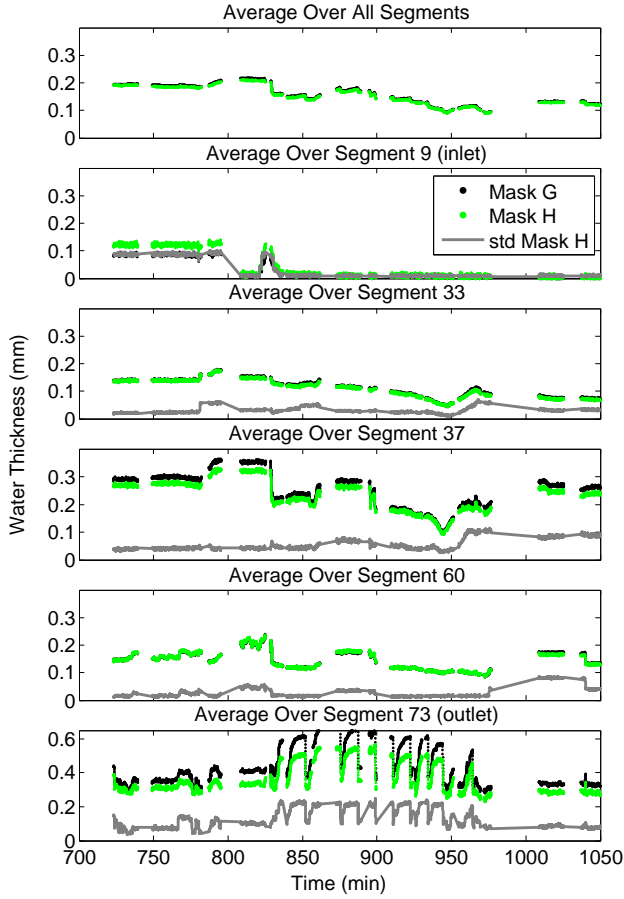


Figure 5. Measured average liquid water thickness in the combined membrane/GDL layer for the entire active area (top subplot) and within selected segments (subsequent subplots) from the same data set shown in Fig 6.

the masses calculated for each of the 81 segments, according to

$$\bar{M}_{GDLMB}^W = \rho_l A_P \sum_{i=1}^{81} N_{P,AA}[i] H[i], \quad (5)$$

$$\bar{M}_{AnCh}^W = \rho_l A_P \sum_{i=1}^{81} N_{P,AnCh}[i] (E[i] - H[i]), \quad (6)$$

$$\bar{M}_{CaCh}^W = \rho_l A_P \sum_{i=1}^{81} N_{P,CaCh}[i] (F[i] - H[i]), \quad (7)$$

where ρ_l is the density of water; A_P is the area of the fuel cell corresponding to a single pixel in the detector; $N_{P,AA}[i]$, $N_{P,AnCh}[i]$ and $N_{P,CaCh}[i]$ are the number of pixels defining the active area, anode channel and cathode channel respectively and $H[i]$, $E[i]$ and $F[i]$ are the measured average water thickness in segment

i for each of the corresponding masks, where the thickness is given by Eqn. (3). The results of this image processing and data analysis are shown in Fig. 6.

Three dimensional computational models have demonstrated the possibility of a non-uniform liquid water distribution inside the GDL, with a buildup of water in regions underneath channel lands [17, 26]. If the true water distribution in the GDL is concentrated under the lands, then the previous assumptions would lead to an underestimate of the amount of liquid water in the channel, and an overestimate of the GDL water content. Therefore this data analysis method represents a lower bound on the mass of accumulated water in the channels, and an upper bound on the mass of water in the GDL.

Local averaging combined with masking yield more accurate results than simply averaging the masked regions over the entire active area due to the non-uniform distribution of water within the cell. The percent difference between the total liquid water mass, and the estimated mass calculated via masked local averages, $\bar{M}_{AnCh}^W + \bar{M}_{CaCh}^W + \bar{M}_{GDLMB}^W$, is less than 2%, indicating that the relative uncertainty introduced by the assumption of a uniform water thickness in the combined membrane and GDL layer for each segment is small. Therefore we have a high level of confidence using the locally averaged and masked data to infer the mass of liquid water in each of the three layers; anode channel, cathode channel and combined membrane GDL.

4 Experimental Results

The neutron imaging data were collected over 4 continuous days of testing (42 hours), for the range of operating conditions summarized in Table 2. The same cell was used throughout all the experiments at various current densities, air stoichiometric ratios, cathode relative humidities and cell temperatures. Control of the fuel cell endplate temperature and cathode bubbler temperature was used to achieve the desired cathode inlet relative humidity. The pressure regulated supply of dry hydrogen gas used for the anode was not humidified.

Relatively low current densities were used than typically reported in the literature. These low-to-medium current density conditions are interesting in portable and mobile application where the system typically idles for a significant time. They also are conditions for which anode flooding is most predominant. At higher current density electro-osmotic drag tends to dry out the anode [31].

Figure. 6 shows the data from one of our full days of testing (6 hrs continuous operation). This data illustrates how stack operating conditions can drive the system from a state of cathode channel flooding to anode channel flooding at low-medium current density. The first subplot of Fig. 6 shows the mass of liquid water in each of the four mutually disjoint masked regions, described in Sec 3.2, over the entire active area. The next 3 subplots show the estimated liquid water mass in each of the

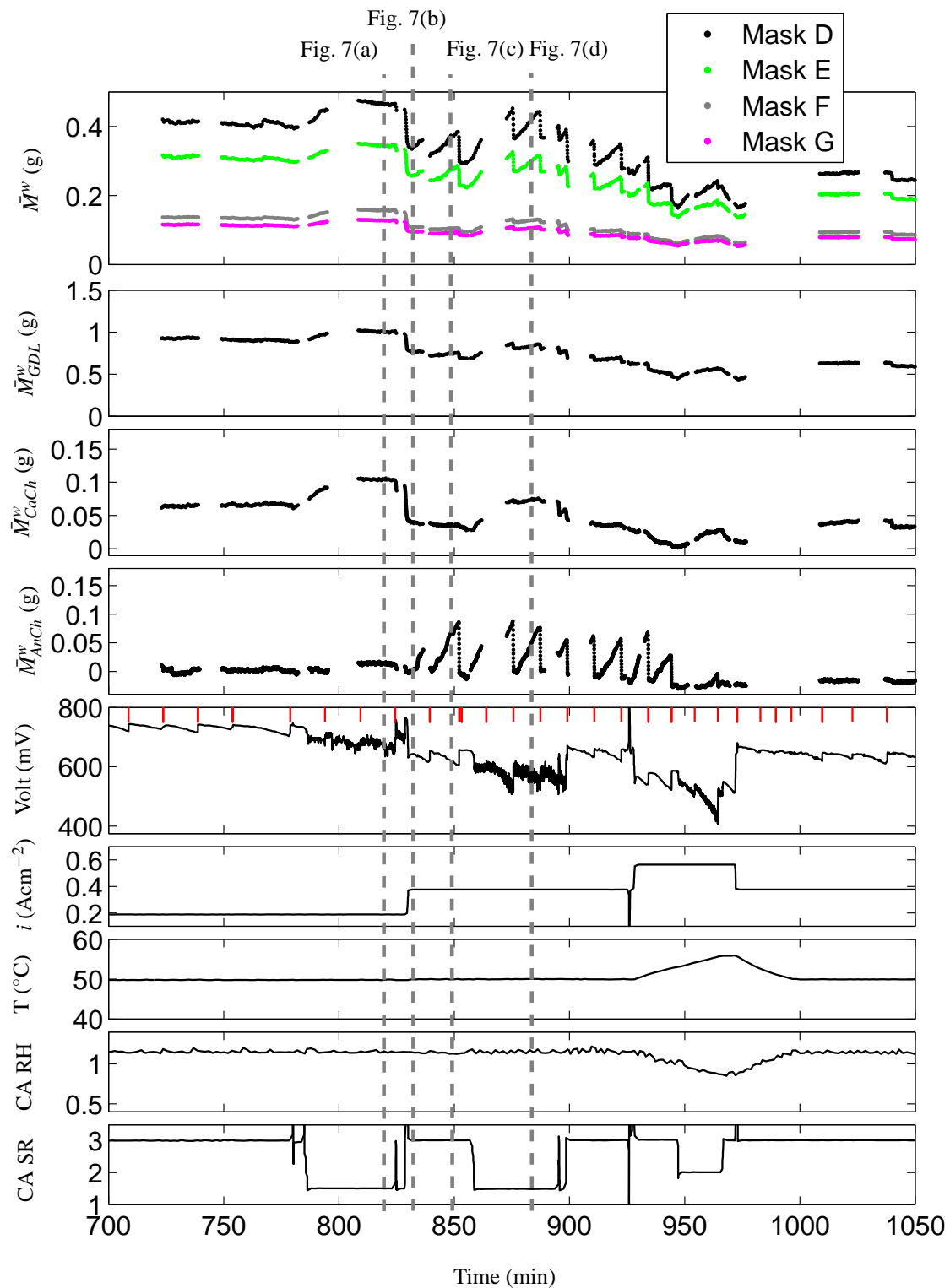


Figure 6. Measured total liquid water mass, estimated membrane/GDL and channel liquid water masses, voltage, current, temperature, cathode stoichiometric ratio, and cathode inlet relative humidity; fully humidified cathode gas (air) and dry hydrogen inlet. Red vertical lines in the voltage subplot indicate an anode purge event

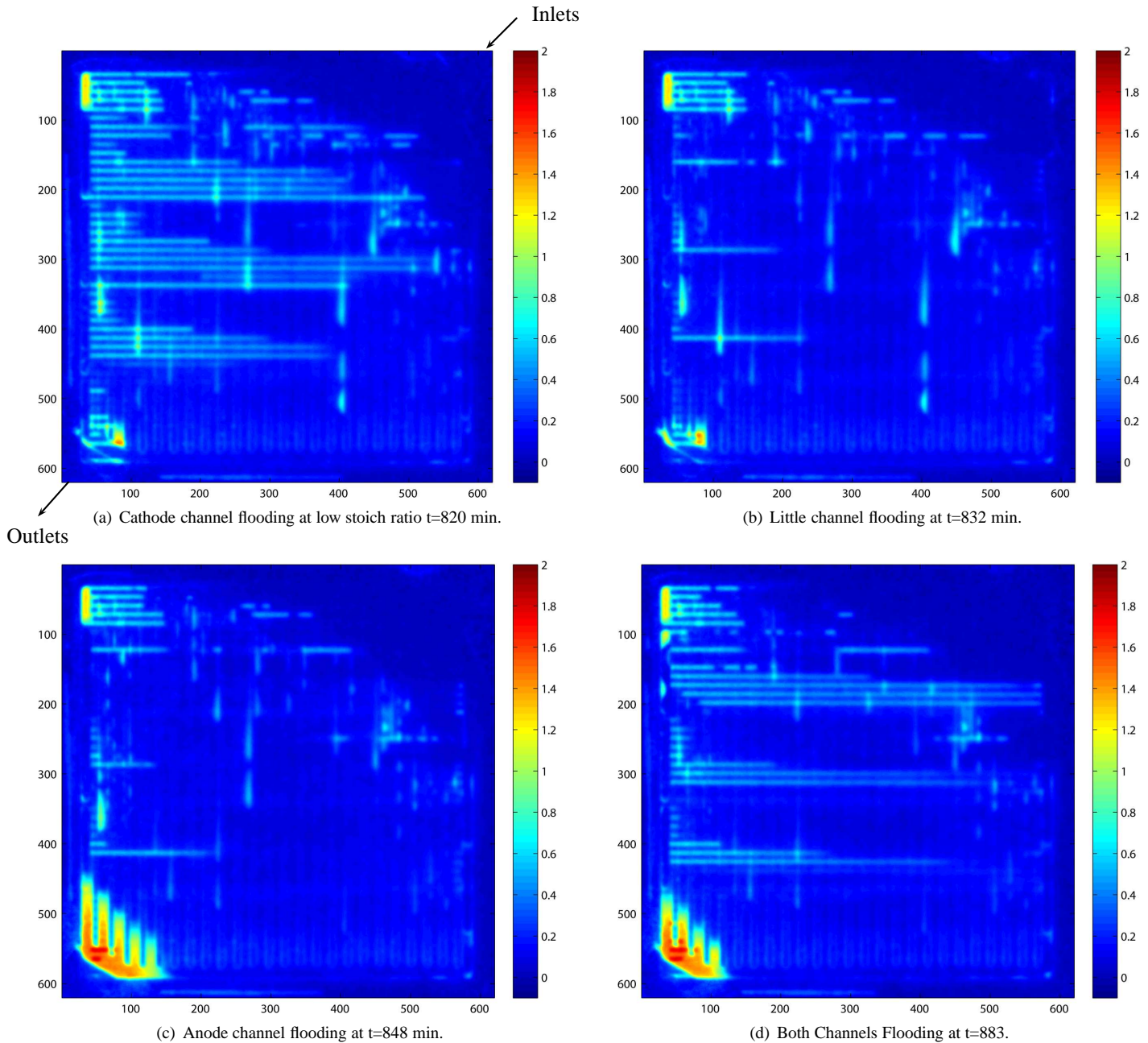


Figure 7. Processed neutron images showing liquid water thickness (mm) under a variety of conditions.

three layers (anode channel, cathode channel and the combined membrane/GDL layer). The last 4 subplots of this figure display the important operating conditions, which are typical model inputs [8]; current density ($A\ cm^{-2}$), end plate cell temperature ($^{\circ}C$), cathode inlet relative humidity and cathode stoichiometric ratio.

One can notice that our operating temp is also lower than

PEMFCs are intended for, but this range was not intentional. Due to the software temperature calibration, the intended operating conditions were not attained and the cell was operated at a temperature colder than desired. The thermocouple was re-calibrated after the experiment, and the corrected temperature is presented in the data. Another consequence of this, is that the bubbler temperature was higher than the fuel cell temperature, causing the es-

Parameter	Operating Range
Anode inlet RH	0
Cathode inlet RH	40% - 100%
Anode Pressure	123.6 kPa absolute
Cathode Pressure	120-125 kPa absolute
Cell Temperature	40,50,60 °C
Cell Current	0 - 30 A, 0-566 mA cm ⁻²

Table 2. Cell operating conditions

timated cathode inlet relative humidities to be sometimes greater than one (see subplot 8, Fig. 6).

The cell is initially operated at low current density (subplot 6) and high cathode stoichiometric ratio (subplot 9). Heaters are used to maintain the end-plate temperature at 50 °C (subplot 7). At $t=783$ min the cathode stoichiometry is decreased and water begins to accumulate in the cell as seen in Fig. 6. Cathode channel flooding is evident in the neutron radiographs, which can be seen in Fig. 7(a) at $t=820$ min, and the voltage fluctuates rapidly. This fluctuation in voltage is likely due to the decrease in catalyst oxygen partial pressure as the cathode channels are intermittently plugged with water. Figure 7(a) also shows the buildup of liquid water after the 180 degree bends in the cathode semi-serpentine flow path as predicted by [32]. However, the water in the cathode channel accumulated only on the left hand side of the image, which corresponds to the “down hill” turnarounds when viewed in the original orientation as shown in Fig. 2. This indicates that when considering 2-D and 3-D models, the orientation of the cell and the effects of gravity may have a non-negligible effect on the location of liquid water buildup within the channels.

Just before $t=825$ min the cathode is surged removing liquid water from the cathode channels, and a sustained voltage recovery of 25 mV is observed. Following the surge, the current density and stoichiometry are both increased. The higher cathode gas velocity more readily removes liquid water from the cathode channel, as seen in Fig. 7(b) at $t=832$ min. This new operating condition eventually leads to anode channel flooding, shown in Fig. 7(c). At $t=858$ min the cathode stoichiometry is again decreased leading to a condition in which both anode and cathode channel flooding is detected, as seen in Fig. 7(d).

The liquid water dynamics are very sensitive to temperature [23], and temperature transients. During the first two days of testing, no external cooling devices were used, and the cell was typically operated under conditions for which the end-plate heaters were required to maintain the desired operating temperature of the aluminum end plates. At $t=925$ min a slow temperature rise of about 5 degrees was measured at the end plates following the current density increase to 566 mA cm⁻². At this higher load level, the cell is unable to maintain a low tempera-

ture by passive cooling. Moreover, the current increase causes a large spatial gradient in temperature. The thermal history of the membrane is very important for modeling the membrane water uptake and conductivity [16, 33]. This thermal history may account for the absence of anode flooding following the return to lower current density and nominal temperature at $t=1000$ min in Fig. 6, for conditions which previously exhibited anode channel flooding.

In testing other conditions, which are not shown in this paper, at higher temperature (60°C) and low cathode RH (40%), anode channel flooding was no longer detected in the neutron images. For these conditions, the total water content in the GDL decreases significantly, about half that of case with fully humidified cathode inlet. Since the water carrying capacity of air increases exponentially with temperature, and therefore can remove far more liquid water under these conditions [23]. At lower current density, 189 mA cm⁻², the liquid water accumulation in the anode channels was distributed throughout the entire active area, which suggests that the anode gas flow rate at low current density is not sufficient to push water to the end of the cell were it can be removed by purging. This is seen in the buildup of liquid water mass in the anode channel which is insensitive to anode purges. At higher current densities, there is a greater hydrogen flow rate and water collects near the end of the anode channels, as shown in Fig. 7(c), and repeatable liquid water transients occur. Data at lower cathode inlet relative humidity (70%), also resulted in anode channel flooding.

4.1 Anode Channel Water Flooding and Voltage Response

The neutron imaging data, with the applied masking techniques, shows the amount of liquid water in the anode channel. A close investigation of this data shows many conditions with anode channel flooding and not cathode channel flooding. These conditions have a predictable and repeatable voltage degradation and the pattern matches exactly the water accumulation in the anode channel. Fig. 8 shows the water distribution for a typical purge cycle. The red vertical lines shown in the voltage subplot indicate anode purge events. Following an anode purge, all of the liquid water in the anode channel is removed, then slowly accumulates until the next purge event. This buildup of liquid water is well correlated with the observed recoverable voltage degradation of approximately 50 mV between purges. Note, that there is little change in the cathode channel water mass between or during purges, which also corroborates a simple water flooding model developed and published in [8].

Following the anode purge, a cathode surge (a temporary increase in cathode excess air) was conducted at approximately 3963 min. During the surge, the cell voltage increases due to the higher oxygen partial pressure. However, after the cathode flow rate is restored, the voltage returns to its previous value.

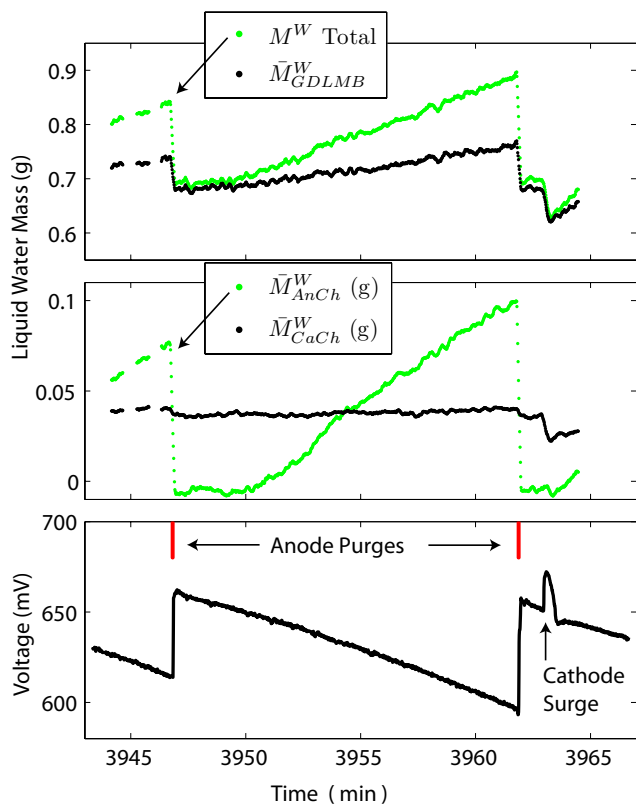


Figure 8. Measured cell voltage degradation and liquid water mass accumulation between anode purges, taken from the third data set. These experiments were conducted with fully humidified air at a current density of 378 mA cm^{-2} , a cell operating temperature of $50 \text{ }^\circ\text{C}$, and an air stoichiometry of 300%.

The mass of liquid water in the cathode channel decreases as a result of the increased water removal rate with higher gas flow rate during the surge. Even when the cathode surge event occurs just preceding the anode purge event, the voltage continues to degrade at the same rate as experienced before cathode surge. These results indicate that liquid water in cathode channel has little effect on voltage under these conditions. In contrast, following the two anode purges at 3947 min and 3962 min, the voltage recovery is significant and sustained until liquid water begins to accumulate in the anode channel again. There exist other operating conditions where a sustained voltage recovery occurs following a cathode surge, indicating cathode flooding. Therefore, the voltage response during cathode surges and anode purges can be used as a diagnostic tool to determine which channel volume has accumulated liquid water.

A strong correlation between voltage and anode channel water was observed at low to medium current density under a variety of operating conditions. However, the hypothesis of a direct effect of anode channel water mass accumulation on voltage is

controversial as most existing models examine the effect of liquid water accumulation in the cathode GDL-Catalyst interface on voltage [2, 14, 15, 34] under flow through conditions. It has been argued that the properties of the GDL allow for significant water accumulation before oxygen mass transport limitations are reached, especially at low current densities [15].

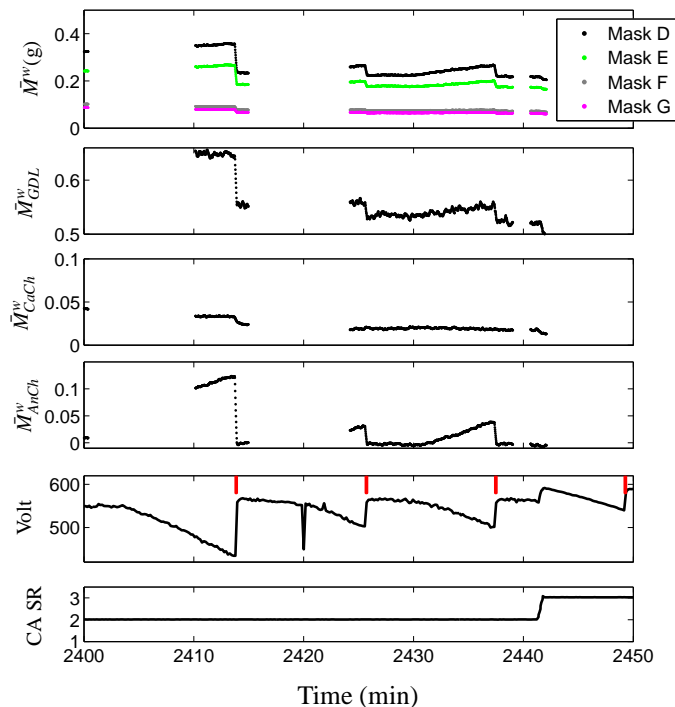


Figure 9. Voltage is well correlated with anode liquid water two slope behavior at $60 \text{ }^\circ\text{C}$, 566 mA cm^{-2} and with a 75% relative humidity for cathode gas stream at 200% stoich.

Figure 9 illustrates a distinctive two slope behavior in anode channel liquid water accumulation which is well correlated with the shape of the voltage degradation. This behavior can be explained by removal of liquid water from the anode GDL, which causes the local liquid water saturation to drop below the immobile limit [35], and interrupting the flow of liquid water into the channel. After a period of time, the level of water in the anode GDL reaches saturation and liquid one again begins to flow into the channel, where it accumulates due to the dead-ended channel. If cathode catalyst flooding was responsible for the observed voltage degradation, the anode purge would have to be capable of removing liquid water from the cathode catalyst layer through the membrane and anode GDL, which is not likely. In addition, the voltage degradation caused by cathode catalyst flooding is not expected to exhibit a two slope behavior, since water is generated at the interface and therefore would much more quickly

return to a flooded state.

5 CONCLUSION

Data were collected on a single cell fuel cell at the NIST neutron imaging facility under dead-ended anode operation. Image masks, based on the cell design, were employed to calculate liquid water mass in the gas channels and the combined membrane gas diffusion layer. Periodic anode purge and cathode surge events were conducted to remove liquid water which was accumulating in the gas channels. It was found that anode purges and cathode surges can be employed as a diagnostic tool indicating anode or cathode flooding. Neutron imaging while operating the cell with a dead-ended anode offers the ability to observe the water dynamics and corresponding voltage, during large and repeatable transients. This data is useful for parameterizing and validating transient models that connect liquid water flooding and cell voltage.

The accumulation of liquid water in the anode gas channels was observed even though a pressure regulates supply of dry hydrogen was fed to the cell. The observed voltage degradation follows the anode channel water build-up under conditions where the cathode channel water mass is not growing. The voltage drop and anode channel water buildup both have a similar two slope behavior following an anode purge which indicates that there is a strong correlation between these two variables, which corroborate a simple model of anode flooding presented in [8].

It is likely that nitrogen accumulation in the anode channel, which crosses over from the air supplied cathode through the membrane, also contributes to the measured voltage degradation [36]. In future work, experiments utilizing concurrent measurements of nitrogen accumulation and liquid water on a PEM fuel cell with dead-ended anode will be conducted at NIST. The goal of this research will be to determine the relative amount of voltage degradation attributed to each source (water and nitrogen build-up) so that control strategies can be developed.

ACKNOWLEDGMENT

We gratefully acknowledge funding from the National Science Foundation (CMS 0625610), and the U.S. Department of Energy (DE-FG02-06CH 11300). The neutron imaging data was collected at the National Institute for Science and Technology (NIST), in Gaithersburg, MD.

REFERENCES

- [1] Bellows, R. J., Lin, M. Y., Arif, M., Thompson, A. K., and Jacobson, D., 1999. "Neutron Imaging Technique for In Situ Measurement of Water Transport Gradients within Nafion in Polymer Electrolyte Fuel Cells". *J. Electrochem. Soc.*, **146**(3), pp. 1099–1103.
- [2] Chuang, P. A., Turhan, A., Heller, A. K., Brenizer, J. S., Trabold, T. A., and Mench, M. M., 2005. "THE NATURE OF FLOODING AND DRYING IN POLYMER ELECTROLYTE FUEL CELLS". In Third International Conference on Fuel Cell Science, Engineering and Technology.
- [3] Chen, Y.-S., Peng, H., Hussey, D. S., Jacobson, D. L., Tran, D. T., Abdel-Baset, T., and Biernacki, M., 2007. "Water distribution measurement for a PEMFC through neutron radiography". *J. Power Sources*, **170**(2), July, pp. 376–386.
- [4] St-Pierre, J., Wilkinson, D. P., Knights, S., and Bos, M., 2000. "Relationships between water management, contamination and lifetime degradation in PEFC". *Journal of New materials for Electrochemical Systems*, **3**, pp. 99–106.
- [5] Meyers, J. P., and Darling, R. M., 2006. "Model of Carbon Corrosion in PEM Fuel Cells". *J. Electrochem. Soc.*, **153**(8), Aug., pp. A1432–A1442.
- [6] Arcak, M., Gorgun, H., Pedersen, L., and Varigonda, S., 2004. "A nonlinear observer design for fuel cell hydrogen estimation". *IEEE Trans. Control Syst. Technol.*, **12**(1), pp. 101–110.
- [7] Pukrushpan, J., Stefanopoulou, A., Varigonda, S., Pedersen, L., Ghosh, S., and Peng, H., 2005. "Control of natural gas catalytic partial oxidation for hydrogen generation in fuel cell applications". *IEEE Trans. Control Syst. Technol.*, **13**(1), pp. 3–14.
- [8] McKay, D. A., Siegel, J. B., Ott, W., and Stefanopoulou, A. G., 2008. "Parameterization and Prediction of Temporal Fuel Cell Voltage Behavior During Flooding and Drying Conditions". *J. Power Sources*, **178**, March, pp. 207–222.
- [9] Siegel, J. B., McKay, D. A., and Stefanopoulou, A. G., 2008. "Modeling and visualization of fuel cell water dynamics using neutron imaging". In 2008 American Control Conference.
- [10] Natarajan, D., and Nguyen, T., 2002. "Three-dimensional effects of liquid water flooding in the cathode of a PEM fuel cell". *J. Power Sources*, **115**, pp. 66–80.
- [11] Pasaogullari, U., and Wang, C.-Y., 2005. "Two-Phase Modeling and Flooding Prediction of Polymer Electrolyte Fuel Cells". *J. Electrochem. Soc.*, **152**(2), pp. A380–A390.
- [12] Berning, T., and Djilali, N., 2003. "A 3D, Multiphase, Multicomponent Model of the Cathode and Anode of a PEM Fuel Cell". *J. Electrochem. Soc.*, **150**(12), Dec., pp. A1589–A1598.
- [13] Wang, Y., and Wang, C., 2007. "Two-phase Transients of Polymer Electrolyte Fuel Cells". *J. Electrochem. Soc.*, **154**(7), pp. B636–B643.
- [14] Berg, P., Promislow, K., Pierre, J. S., Stumper, J., and Wetton, B., 2004. "Water Management in PEM Fuel Cells". *J. Electrochem. Soc.*, **151**(3).
- [15] Lin, G., He, W., and Nguyen, T. V., 2004. "Modeling Liquid Water Effects in the Gas Diffusion and Catalyst Layers of the Cathode of a PEM Fuel Cell". *J. Electrochem. Soc.*,

- 151**(12), pp. A1999–A2006.
- [16] Weber, A., and Newman, J., 2004. “Modeling Transport in Polymer-Electrolyte Fuel Cells”. *Chemical Reviews*, **104**(10), pp. 4679–4726.
- [17] Ju, H., Luo, G., and Wang, C.-Y., 2007. “Probing Liquid Water Saturation in Diffusion Media of Polymer Electrolyte Fuel Cells”. *J. Electrochem. Soc.*, **154**(2), Feb., pp. B218–B228.
- [18] Kramer, D., Zhang, J., Shimoi, R., Lehmann, E., Wokaun, A., Shinohara, K., and Scherer, G., 2005. “In situ diagnostic of two-phase flow phenomena in polymer electrolyte fuel cells by neutron imaging Part A. Experimental, data treatment, and quantification”. *Electrochimica Acta*, **50**, pp. 2603–2614.
- [19] Trabold, T., Owejan, J., Jacobsen, D., Arif, M., and Huffman, P., 2006. “In Situ Investigation of Water Transport in an Operating PEM Fuel Cell Using Neutron Radiography: Part I-Experimental Method and Serpentine Flow Field Results”. *Int. J. Heat Mass Transfer*, **49**, pp. 4712–4720.
- [20] Satija, R., Jacobson, D. L., Arif, M., and Werner, S. A., 2004. “In situ neutron imaging technique for evaluation of water management systems in operating PEM fuel cells”. *J. Power Sources*, **129**(2), Apr., pp. 238–245.
- [21] Turhan, A., Heller, K., Brenizer, J., and Mench, M., 2006. “Quantification of liquid water accumulation and distribution in a polymer electrolyte fuel cell using neutron imaging”. *J. Power Sources*, **160**, pp. 1195–1203.
- [22] Yoshizawa, K., Ikezoe, K., Tasaki, Y., Kramer, D., Lehmann, E. H., and Scherer, G. G., 2008. “Analysis of Gas Diffusion Layer and Flow-Field Design in a PEMFC Using Neutron Radiography”. *J. Electrochem. Soc.*, **155**(3), Mar., pp. B223–B227.
- [23] Hickner, M. A., Siegel, N. P., Chen, K. S., Hussey, D. S., Jacobson, D. L., and Arif, M., 2008. “Understanding Liquid Water Distribution and Removal Phenomena in an Operating PEMFC via Neutron Radiography”. *J. Electrochem. Soc.*, **155**(3), Mar., pp. B294–B302.
- [24] McKay, D. A., Ott, W. T., and Stefanopoulou, A., 2005. “Modeling, Parameter Identification, and Validation of Water Dynamics for a Fuel Cell Stack”. In Proceedings of 2005 ASME International Mechanical Engineering Congress & Exposition, Vol. IMECE 2005-81484.
- [25] Woo, C. H., and Benziger, J., 2007. “PEM fuel cell current regulation by fuel feed control”. *Chemical Engineering Science*, **62**(4), Feb., pp. 957–968.
- [26] Natarajan, D., and Van Nguyen, T., 2001. “A Two-Dimensional, Two-Phase, Multicomponent, Transient Model for the Cathode of a Proton Exchange Membrane Fuel Cell Using Conventional Gas Distributors”. *J. Electrochem. Soc.*, **148**(12), Dec., pp. A1324–A1335.
- [27] Hussey, D., Jacobson, D., and Arif, M., 2007. “In situ fuel cell water metrology at the NIST neutron imaging facility”. *Proceedings of the ASME International Conference on Fuel Cell Science, Engineering and Technology*.
- [28] Hickner, M., Siegel, N., Chen, K., McBrayer, D., Hussey, D., Jacobson, D., and Arif, M., 2006. “Real-Time Imaging of Liquid Water in an Operating Proton Exchange Membrane Fuel Cell”. *J. Electrochem. Soc.*, **153**, pp. A902–A908.
- [29] Hassanein, R., Lehmann, E., and Vontobel, P., 2005. “Methods of scattering corrections for quantitative neutron radiography”. *Nucl. Instrum. Methods Phys. Res., Sect. A*, **542**(1-3), Apr., pp. 353–360.
- [30] McCain, B. A., Stefanopoulou, A. G., and Kolmanovsky, I. V., 12-14 Dec. 2007. “A multi-component spatially-distributed model of two-phase flow for estimation and control of fuel cell water dynamics”. In Decision and Control, 2007 46th IEEE Conference on, pp. 584–589.
- [31] Karnik, A. Y., Stefanopoulou, A. G., and Sun, J., 2007. “Water equilibria and management using a two-volume model of a polymer electrolyte fuel cell”. *J. Power Sources*, **164**(2), Feb., pp. 590–605.
- [32] Pekula, N., Heller, K., Chuang, P., Turhan, A., Mench, M., Brenizer, J., and Unlu, K., 2005. “Study of water distribution and transport in a polymer electrolyte fuel cell using neutron imaging”. *Nucl. Instrum. Methods Phys. Res., Sect. A, Proceedings of the Fifth International Topical Meeting on Neutron Radiography*, **542**, pp. 134–141.
- [33] Onishi, L., Prausnitz, J., and Newman, J., 2007. “Water-Nafion Equilibria. Absence of Schroeder’s Paradox”. *Journal of Physical Chemistry B*, **111**(34), pp. 10166–10173.
- [34] Ge, S., and Wang, C.-Y., 2007. “Liquid Water Formation and Transport in the PEFC Anode”. *J. Electrochem. Soc.*, **154**(10), Oct., pp. B998–B1005.
- [35] Nam, J., and Kaviani, M., 2003. “Effective diffusivity and water-saturation distribution in single and two-layer PEMFC diffusion medium”. *Int. J. Heat Mass Transfer*, **46**, pp. 4595–4611.
- [36] Kocha, S. S., Yang, J. D., and Yi, J. S., 2006. “Characterization of gas crossover and its implications in PEM fuel cells”. *AIChE Journal*, **52**(5), pp. 1916–1925.